Supplementary Information:

DNA nanostars that self-assemble into core-shell condensate microdroplets

Karuna Skipper[1,2], Shelley F.J. Wickham[1,2,3]

[1] School of Chemistry, The University of Sydney, Sydney, NSW 2006, Australia

[2] The University of Sydney Nano Institute, The University of Sydney, Sydney, NSW 2006, Australia

[3] School of Physics, The University of Sydney, Sydney, NSW 2006, Australia

E-mail: shelley.wickham@sydney.edu.au

Table of Contents

Supplementary Discussion

The molecular and microscale properties of single-phase droplets were explored, demonstrating systematic changes in droplet properties with nanostar shape and SE sequence. Weak SEs (6, 8-weak) resulted in either large asymmetric droplets (SE 6) or extended irregular structures (SE 8-weak) (SI Figure S1-2). SE 6 droplets deformed and flattened on contact with the glass surface (SI Figure S3), with smallest contact angles (3S6 ~ 30°, 4S6 = 65°, 4L6 = 85°, SI Figure S1). Intermediate and strong SEs (SE 8, 8-strong, 10) resulted in droplets of smaller average size with spherical shape and limited deformation on contact with glass (contact angles ~ 110-120°, SI Figure S3). For intermediate SE spherical droplets (SE 8, 8-strong), structural variants with the same SE had decreasing average size in order of 4L, 4S, 3S (SI Figure S2).

These results show that weak SEs (SE 6, 8-weak; TM = 31, 34 °C respectively) produce larger droplets or irregular structures, consistent with a longer active range with more time for fusion events to occur. Droplets were more deformable and liquid-like at room temperature (T_R), indicating $T_G \leq T_R$. Stronger SEs (SE 8, 8-strong, 10; T_M = 49, 52, 54 °C respectively) produced smaller and less polydisperse size droplets, consistent with shorter active ranges and fewer fusion events (SI Figure S4). Droplets deformed less when observed, indicating $T_G > T_R$. For higher strength SEs, the increase in mean radius and size distribution width between 4S and 4L aligns with the previously observed trend of faster growth for larger size nanostars.[18] An increase in size and distribution width from 3S to 4S is similarly consistent with increased valency leading to higher cooperativity and thus a higher T_{PS} and a longer active range.[17] For the most liquid-like droplets (SE 6), the increase in observed contact angle indicates a transition from high to low deformability from 3S, to 4S, then 4L. This is consistent with the expected increase of stability with higher valency (3S < 4S) and suggests that longer arm-length increases stability (4S < 4L). Alternatively, the contact angle between droplet and substrate could be affected by different DNA-DNA and DNA-glass adhesion strengths, or differences in the nanostar packing density.

On the molecular level, we then characterised nanostar size and mobility, and passive partitioning of cargo. First, Dynamic Light Scattering (DLS) of 0-nt SE stars was used to confirm nanostar size decreased in the order 4L > 4S > 3S, as expected from designs (SI Figure S5). Next, Fluorescence Recovery After Photobleaching (FRAP) was used to qualitatively compare internal nanostar mobility (SI Figure S6). Nanostars form a dynamic 3D network in droplets with a mesh size that decreases with valency but increases with arm length.[14] Mobility

of stars within the network gives information on how dynamic and liquid-like the droplet is. In agreement with confocal results, increasing SE strength led to decreased fluorescence recovery, indicating decreased star mobility (6 > 8-weak > 8 = 8-strong = 10). Comparing between weaker SE sequences (6, 8-weak), for the trivalent 3S droplets the fluorescence recovered faster than the tetravalent 4S and 4L, indicating higher star mobility. Finally, passive diffusion of FITC-dextran was used to qualitatively compare droplet mesh size, with lower infiltration of higher molecular weight dextran expected for smaller mesh sizes (SI Figure S7).[14] For all SE tested (8, 8-strong, 10), dextran infiltration was lowest for 4S, while 3S and 4L were indistinguishable. For the 3S star type, 3S8 or 8-strong droplets had lower infiltration than for SE 3S10, while 4S and 4L nanostars had no difference between SEs (SI Figure S8). Decrease of infiltration with decrease of SE length for 3S stars is likely also due to decrease in total star size.

Strand	Sequence (5’ - 3’)
3S-1	CCA CGC TAC GAT GCT GttTGA AGG CAG GAG TGA Ca
3S-2	GTC ACT CCT GCC TTC AttACC TGT CCG CAC CAA Ca
3S-3	GTT GGT GCG GAC AGG TttCAG CAT CGT AGC GTG Ga
Star T_M (^oC)	79.3
ΔG (kcal/mol)	-66.25
4S-1	TGG ACT AAC GGA ACG Gtt AGT CAG GTA TGC CAG Ca
4S-2	GCT GGC ATA CCT GAC Ttt CGC AAA TTT ACA GCG Ca
4S-3	GCG CTG TAA ATT TGC GttCAT CAC TTG GGA CCA Ta
4S-4	ATG GTC CCA AGT GAT Gtt CCG TTC CGT TAG TCC Aa
Star T_M (^oC)	72.5
ΔG (kcal/mol)	-85.32
4L-1	CAG CCG GTT GCC CTT AAG CTG CGa a GC ATC GGC ACA AAC GAC TGC ATC a
4L-2	GAT GCA GTC GTT TGT GCC GAT GCa aGG CTT CGC CTA CAG TCC GGC TCC a
4L-3	GGA GCC GGA CTG TAG GCG AAG CCa aCG CTC GGA GAC ACG ATT GGG CTG a
4L-4	CAG CCC AAT CGT GTC TCC GAG CGa aCG CAG CTT AAG GGC AAC CGG CTG a
Star T_M (^oC)	86.2
ΔG (kcal/mol)	-137.53

SI Table 1: Nanostar arm sequences developed in NUPACK, with the predicted T_M and Gibbs free energy of the full nanostar structure

Strand	Sequence (5’ - 3’)
6 nt SE	–CGA TCG
8 nt SE	–CGA GCT CG
8-A nt SE	–GCG ATC GC
8-B nt SE	–GCT ATA GC
10 nt SE	–CTG AGC TCA G

SI Table 2: Nanostar sticky end sequences

Strand	Sequence (5’ - 3’)
Cy3 connector	TTG ATT GTT TCT CTT TGC GTT TCT–
Cy3 fluorophore	AGA AAC GCA AAG AGA AAC AAT CAA AGT CAG AGG GTA CTT ACC ACC/3Cy3Sp/
Cy5 connector	CTG ATT ATT GTG TGA CAA AAT AA–
Cy5 fluorophore	TTA TTT TGT CAC ACA ATA ATA ATC AGA GAG ATA ACC ATT TTA TAA/3Cy5Sp/
ATTO488 connector	AAG GAC CAC CGC ATC TCT ACA–
ATTO488 fluorophore	TGT AGA GAT GCG GTG GTC CTT/3ATTO488N/

SI Table 3: Sequences of fluorophore connector strands appended to 5’ ends of nanostar arms, and the complementary fluorophore sequences.

Solution	Initial concentration	Final concentration	Volume
DNA strands 1-4*	55 μM	10 μM	4 μL
Fluorophore connector	2.2 μM	0.1 μM	1 μL
Fluorophore	2.2 μM	0.1 μM	1 μL
NaCl	2.75 M	0.5 M	4 μL
Water	-	-	4 μL
Total volume			22 μL

SI Table 4: Volumes required in producing a standard single-star solution. *Trimer nanostars lack strand 4; water is added to maintain solution volume.

	Original		Replacement	
%C	Strand 1	Strand 2	Strand 1	Strand 2
0	4	4		
6.25	3.5	3.5	0.5	0.5
12.5	3	3	1	1
16	2.72	2.72	1.28	1.28
25	2	2	2	2
50			4	4

SI Table 5: Strand replacement in tetravalent stars for 0-50 %C; μL

	Original		Replacement	
%C	Strand 1	Strand 2	Strand 1	Strand 2
0	4	4		
8	3	4	1	
16	2	4	2	
32	2	2	2	2
50	1	1	3	4

SI Table 6: Strand replacement in trivalent stars for 0-50 %C; μL

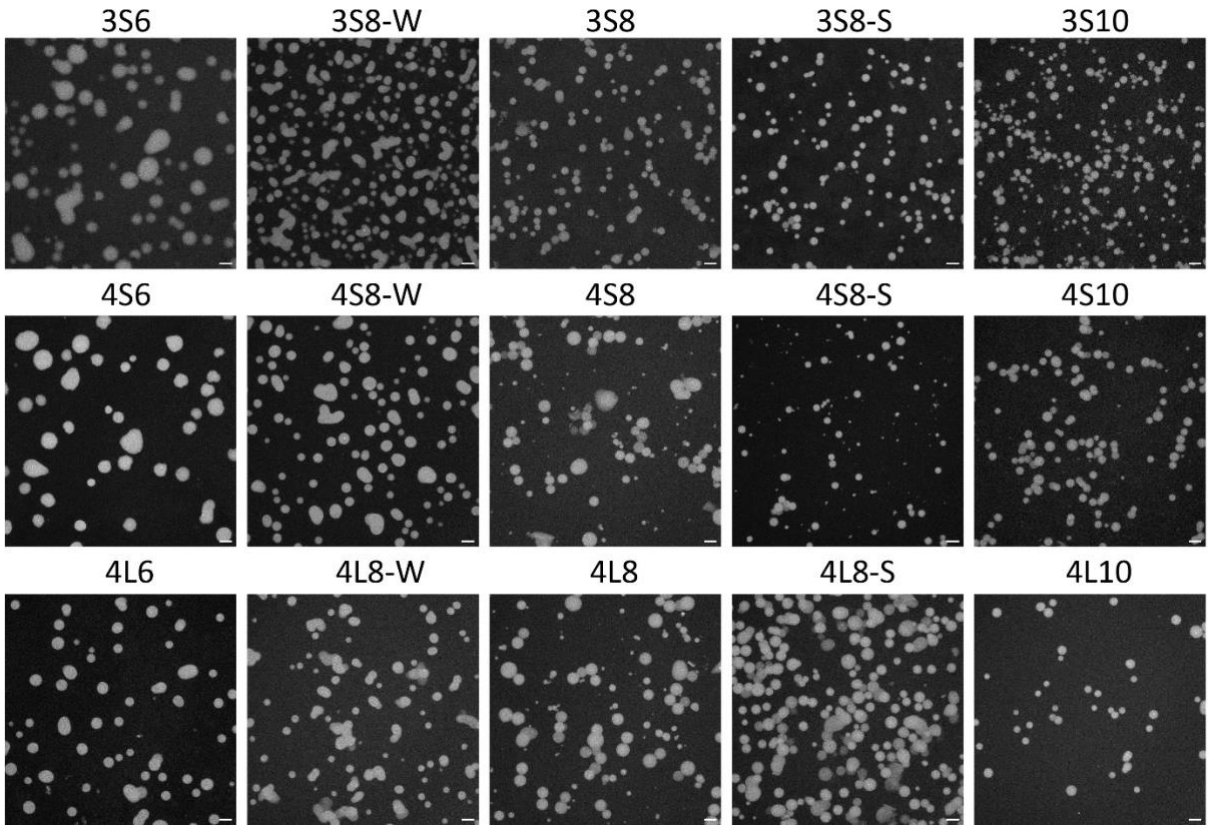

SI Figure 1: Example confocal images of single-phase DNA nanostar droplets, prepared at standard conditions of 10 μM nanostars and 0.5 M NaCl, annealed at 0.5 ^{o}C/min. Scale bars 10 μm.

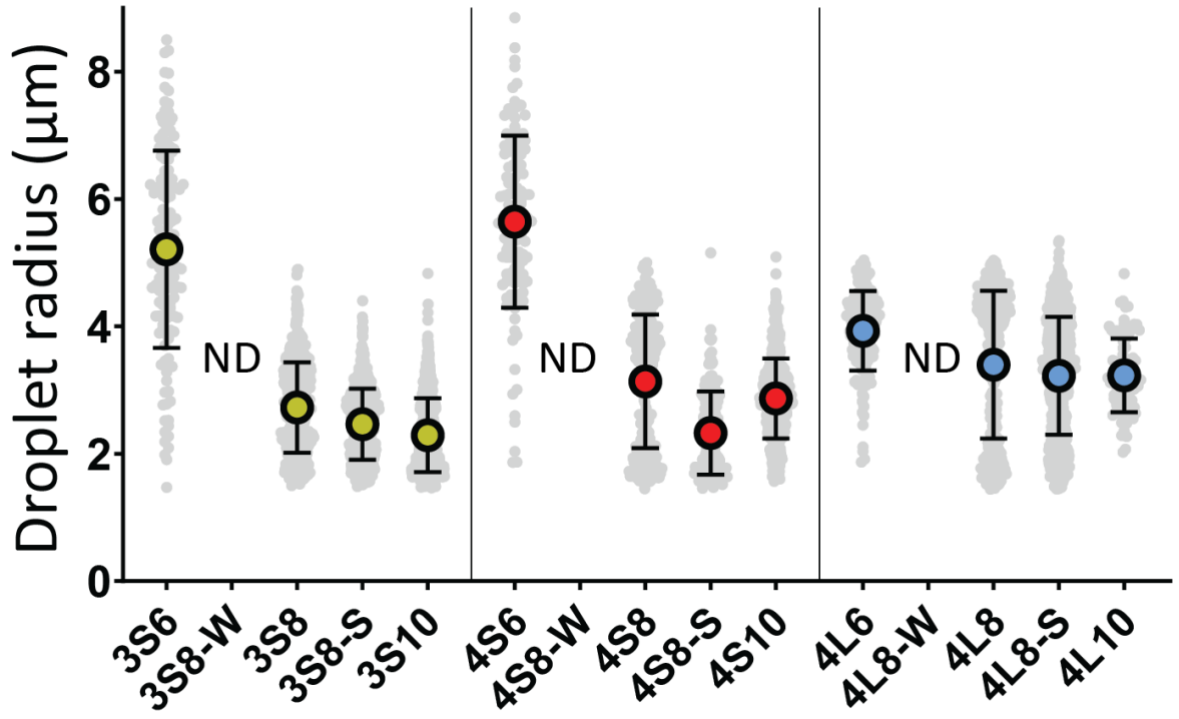

SI Figure 2: Size distribution of bare core-only droplets, measured by confocal microscopy. Droplets with 8W-nt SEs do not form spherical droplets but instead form extended irregular structures that have no well-defined size ('ND').

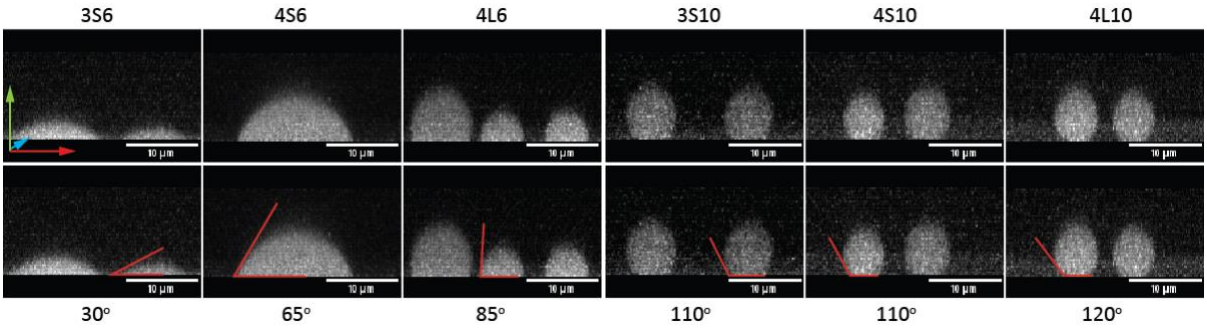

SI Figure 3: Confocal 3D projections of exemplar droplets showing three dimensional projections. In contrast to the spherical 10-nt SE droplets, 3S6, 4S6, and 4L6 droplets have decreased internal contact angles indicating lower relative interfacial tension. Scale bars 10 μm.

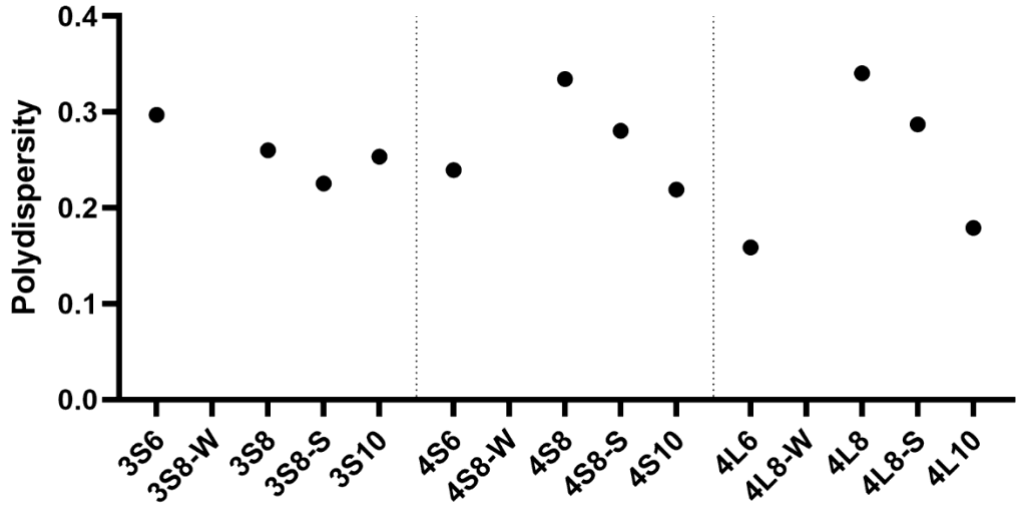

SI Figure 4: Polydispersity index (standard deviation normalised to mean) of bare core-only droplets, showing an increase in uniformity with increasing SE strength (8, 8-strong, 10-nt SEs).

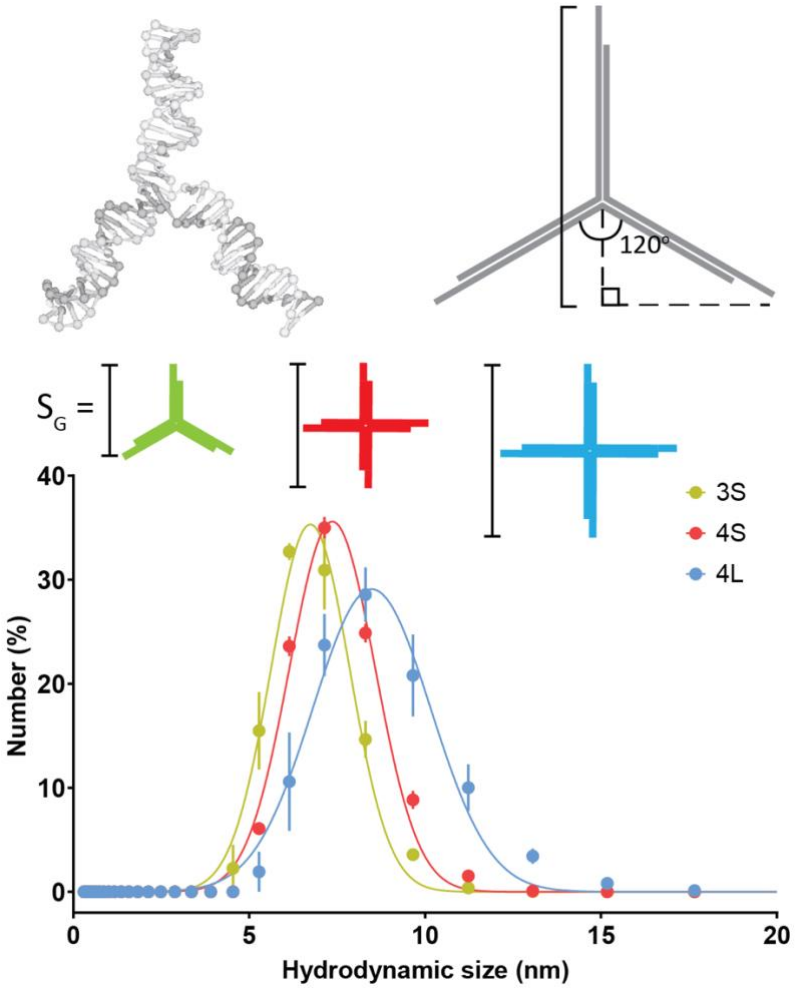

SI Figure 5: Nanostar size characterisation. Top: Nanostar size can be estimated by coarse-grained simulations (oxDNA, left) or geometric approximation (right). Bottom: DLS was used to experimentally measure hydrodynamic size of 3S0, 4S0, and 4L0 nanostars. The measured Dh of the three nanostars were fit to Gaussian functions, excluding measurements above 100 nm, averaged across three replicates. This analysis produced narrowly distributed hydrodynamic sizes for each nanostar, of 6.7 ± 0.3 nm, 7.4 ± 0.1 nm, and 8.5 ± 0.7 nm for 3S, 4S, and 4L, respectively. ANOVA indicated a significant difference between each measured size ($p < 0.0001$), aligning with the expected increase in nanostar size based on valency and arm length. Inset illustrates method used in calculating the geometric size (SG) of nanostars, assuming a flat equilateral triangle in trimer stars and an equal-armed cross in tetramer stars. Values for SG were calculated for all nanostar and SE variants.

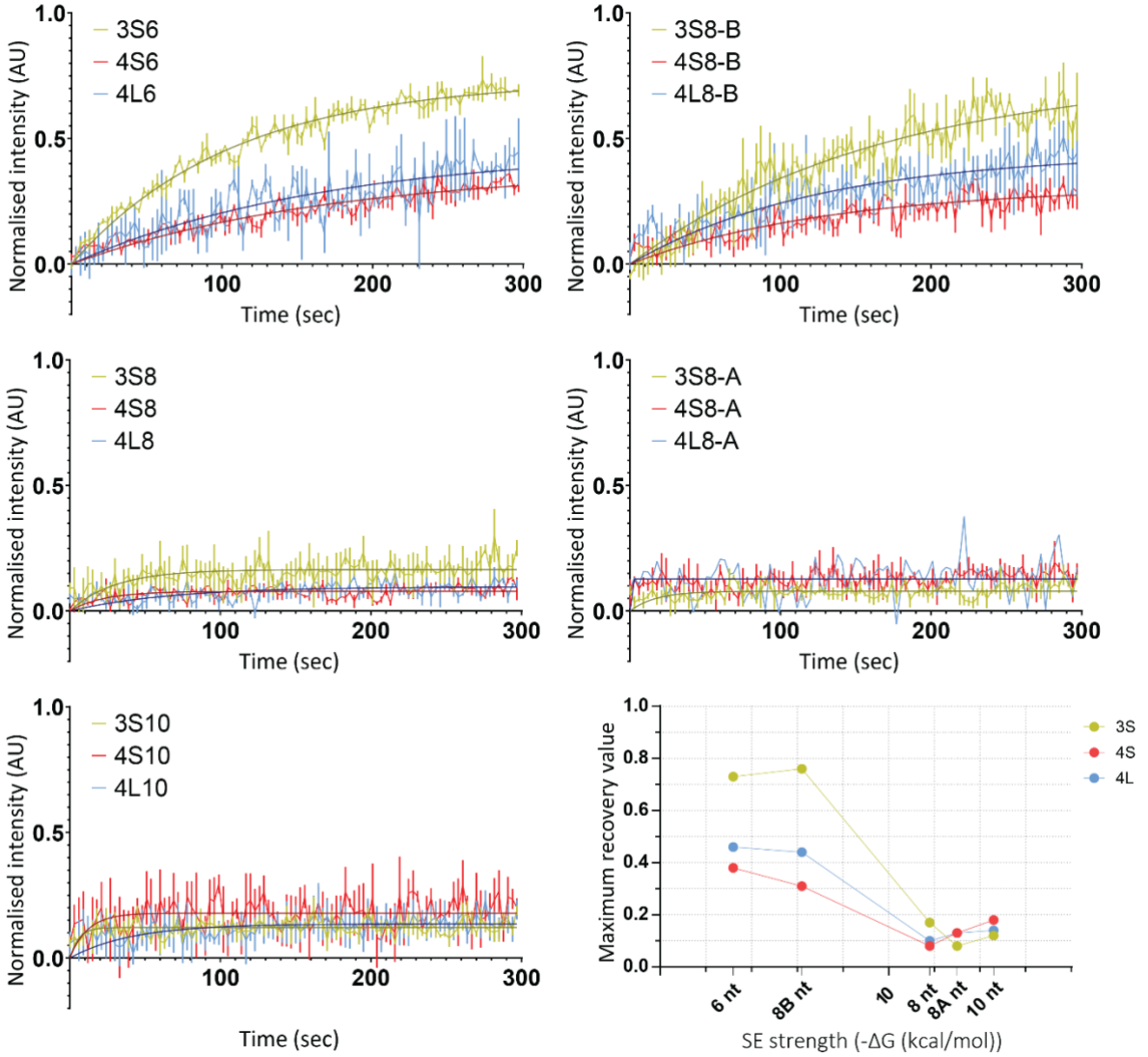

SI Figure 6: Fluorescence recovery after photobleaching curves for droplets prepared under standard conditions (**I-V**). FRAP conducted at 28 °C. Trendline showing fitted data of n = 3 measurements. Error bars showing standard deviation.**VI** Maximum fluorescence recovery values of fit of average FRAP recovery curves

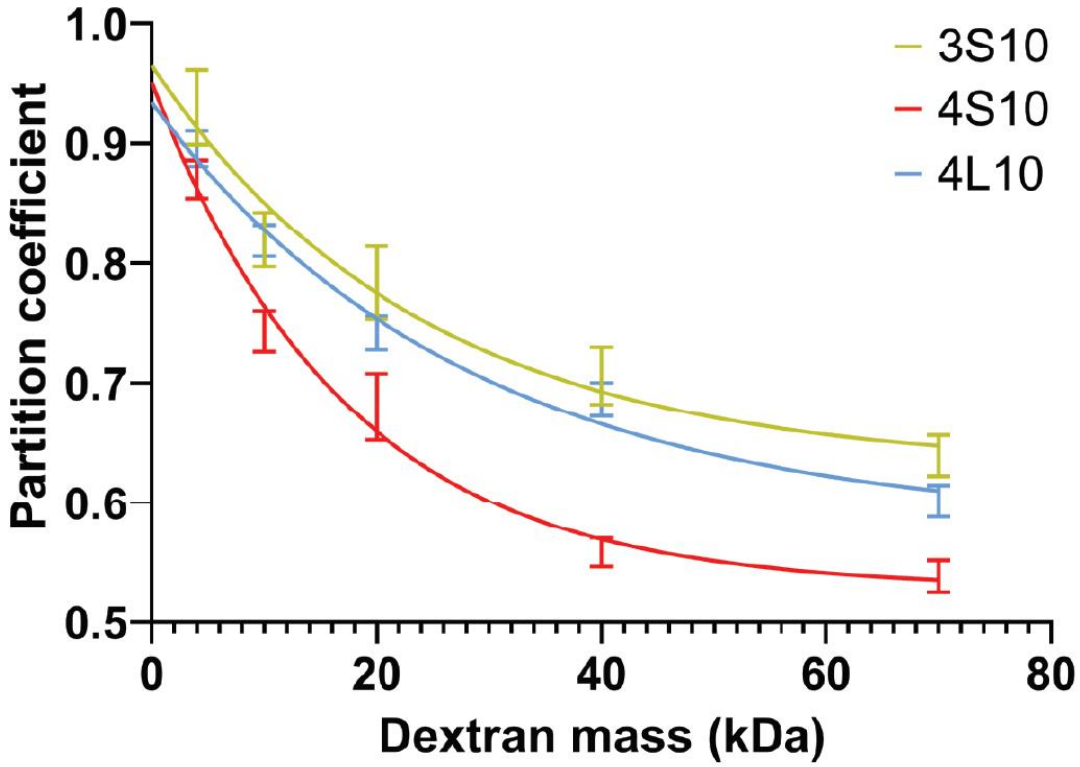

Mass (kDa)	4	10	20	40	70
R_{min} (nm)	10.58	14.36	18.09	22.80	27.47
P ± SD	0.869 ± 0.016	0.743 ±0.017	0.681 ±0.028	0.558 ±0.012	0.538 ±0.013

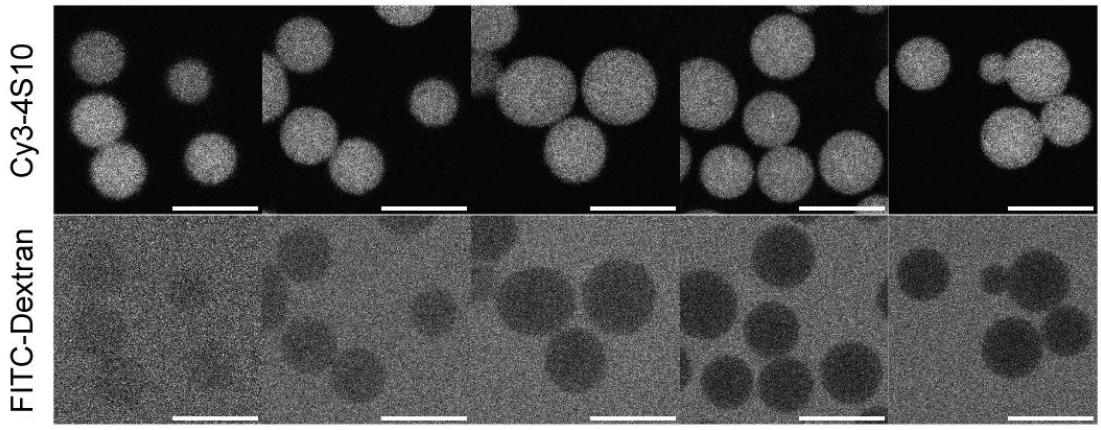

SI Figure 7: Dextran infiltration in 3S10, 4S10, and 4L10 droplets **Top**: measured as ratio of fluorescence intensity of dextran inside and outside of droplets. Average of n = 10 droplets. Curve showing fit to one-phase exponential decay, R2 > 0.91. Error bars showing standard deviation. **Bottom**: Example confocal images of dextran infiltration in 4S10 droplets. Scale bars 10 μm.

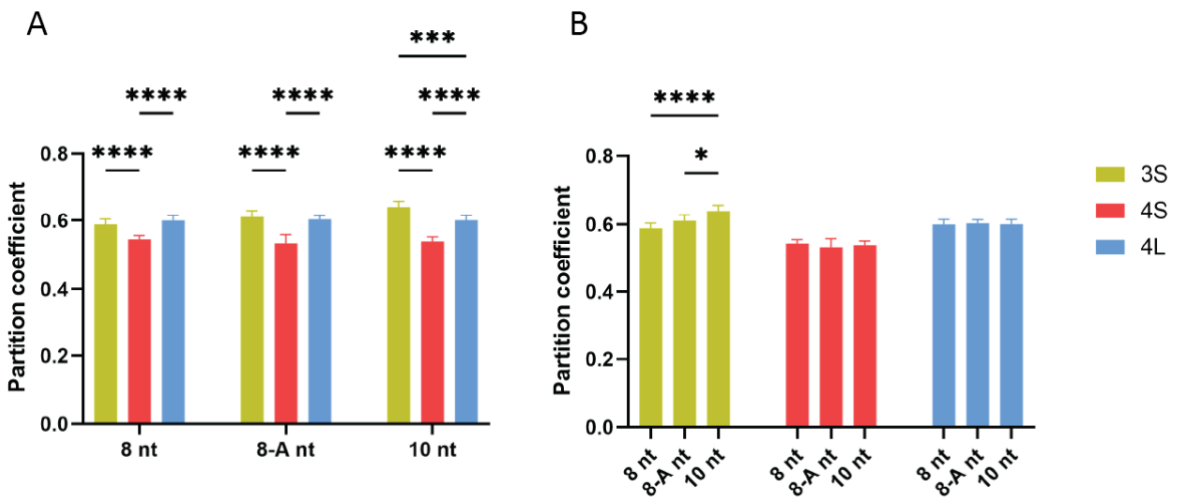

SI Figure 8: Passive Infiltration. Experimentally determined partition coefficients of 70 kD dextran in nanostar droplets. A: When comparing droplets by nanostar sticky end, the partition coefficient in 4S nanostars is significantly lower than in 3S or 4L. B: When comparing droplets by nanostar valency and arm length, no difference is seen between sticky ends for 4S or 4L nanostars, while partitioning in 3S nanostars increases with SE binding strength. Data shown as mean ± SD, with results of Tukey multiple comparisons test statistical analysis, n = 9.

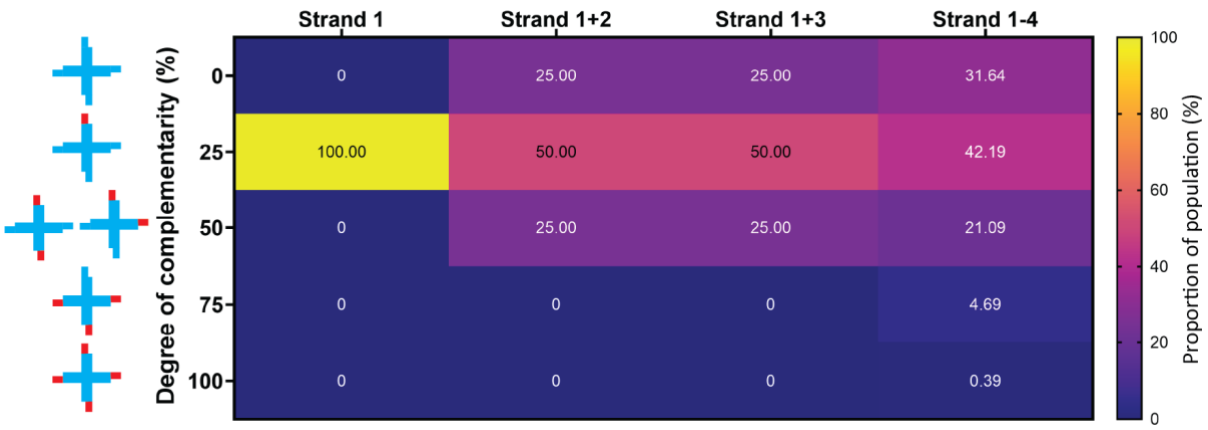

SI Figure 9: Strand Replacement patterns. Variations in the pattern of strand replacement in shell nanostars investigated in a dual tetravalent system. Four forms of shell nanostar sticky end replacement were tested:

• Strand 1: The total replacement of one strand, leading to all nanostars in the system having a single core-complementary SE.

• Strand 1+2: Replacement of half of two different strands, adjacent in placement, creating a population of stars with a normal distribution between 0-50 %C.

• Strand 1+3: Replacement of half of two different strands, opposite in placement, creating a population of stars with a normal distribution between 0-50 %C.

• Strand 1-4: Replacement of one quarter of each strand, creating varieties with an asymmetric distribution of 0-100 %C.

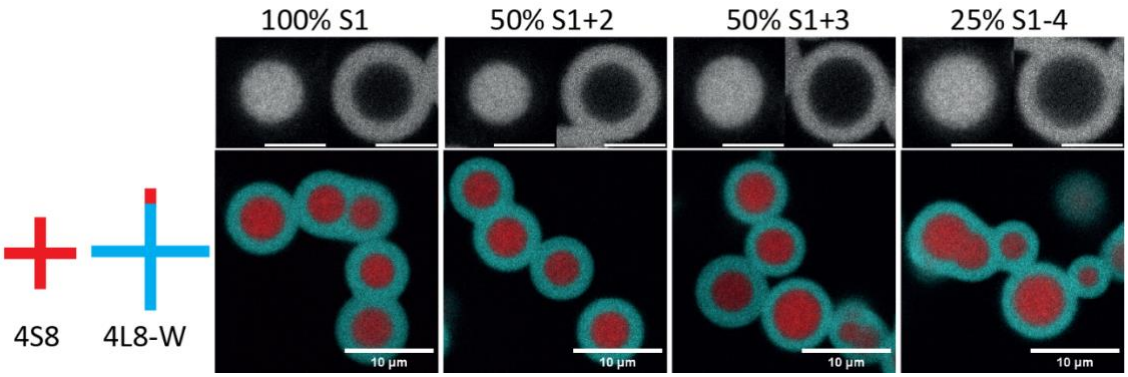

SI Figure 10: SE replacement patterns for 4S8 4L8-weak 25 %C droplets. When imaging, Cy5 fluorophores were applied to the core nanostars and Cy3 to the shell. It was found that regardless of the pattern of sticky end replacement, core-shell structures formed. This suggests that the degree of complementarity between nanostar populations and ΔT_{PS} are the key parameters in determining overall morphology. The case of the total replacement of strand 1, resulting in 100% of shell nanostars having 25% complementarity to the core, demonstrates that an independent surfactant species is not required to initiate this behaviour. Scale bars 10 µm.

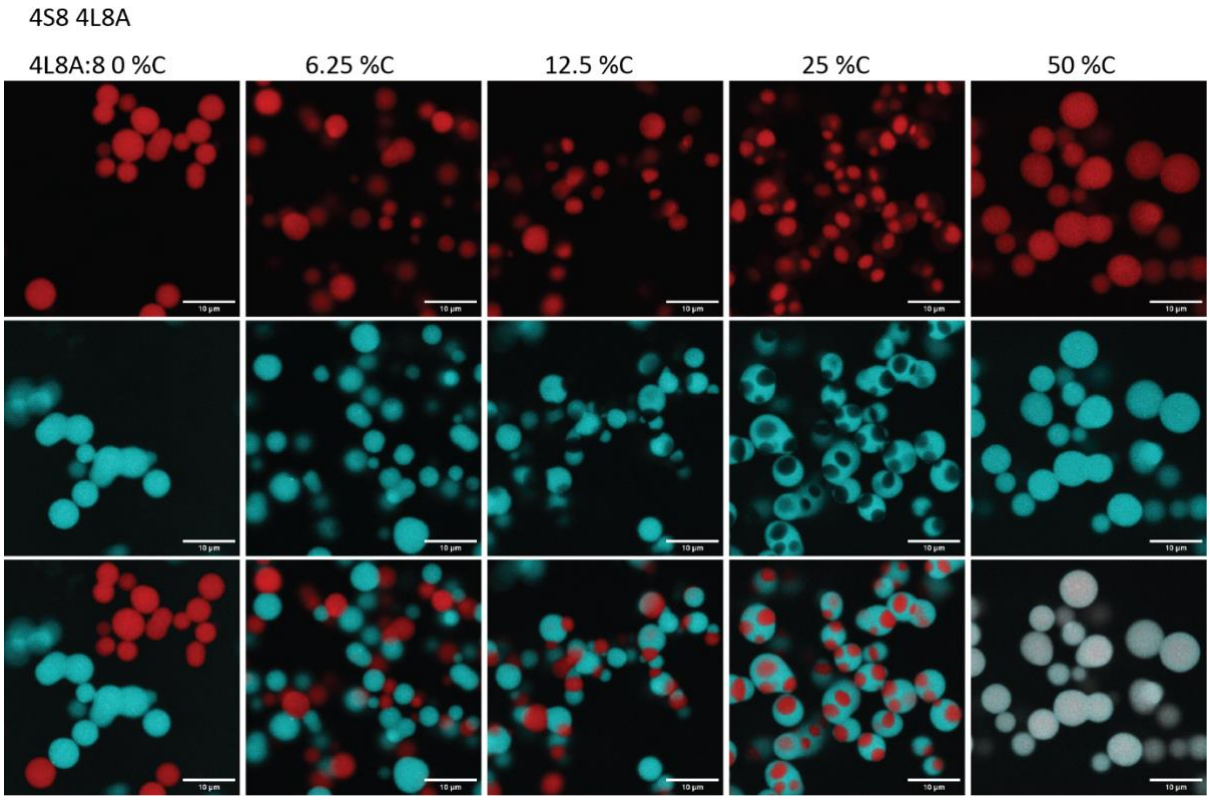

SI Figure 11: Microscale architectures upon increasing complementarity at low ΔTPS, 0.6 ºC, 4S8 and 4L8A, false-coloured red and cyan respectively. At 0 %C, complete separation is seen between populations. At 6.25 and 12.5 %C, an increasing degree of wetting of 4S8 against 4L8A occurs, conferred by the low level of attraction of 4L8A to 4S8. Patchy droplets form at 25 %C, with multiple cores of 4S8 suspended within spheres of 4L8A. At 50 %C, the degree of attraction between nanostar populations leads to mixing of droplet phases. Scale bars 10 μm.

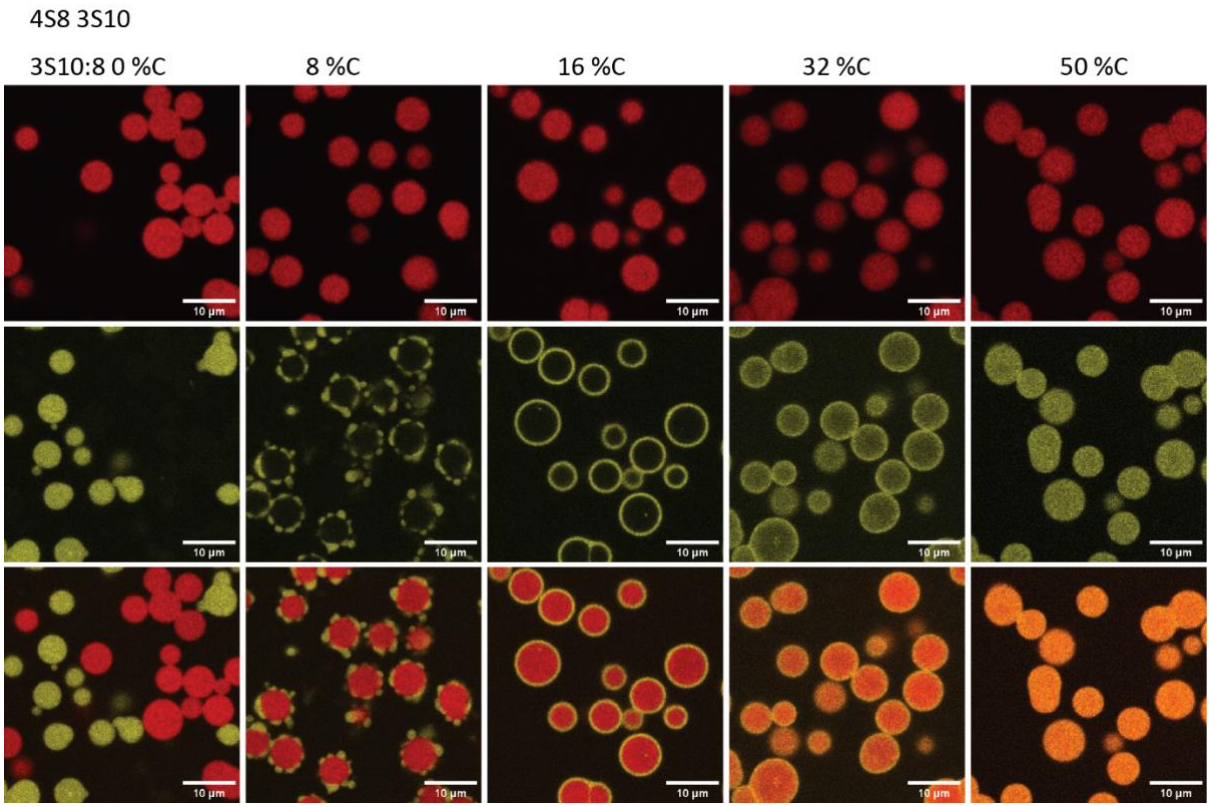

SI Figure 12: Microscale architectures upon increasing complementarity at high ΔTPS, comparing 4S8 3S10 (6.6 ºC). Droplets are false coloured red for 4S8 and yellow for 3S10. At 0 %C, there is complete separation between populations. At low degrees of complementarity, wetting of the lower T_{PS} star occurs against the high T_{PS} core. At 16 %C, core-shell structures form. At 33 %C and above, mixing of phases is observed. Scale bars 10 µm.

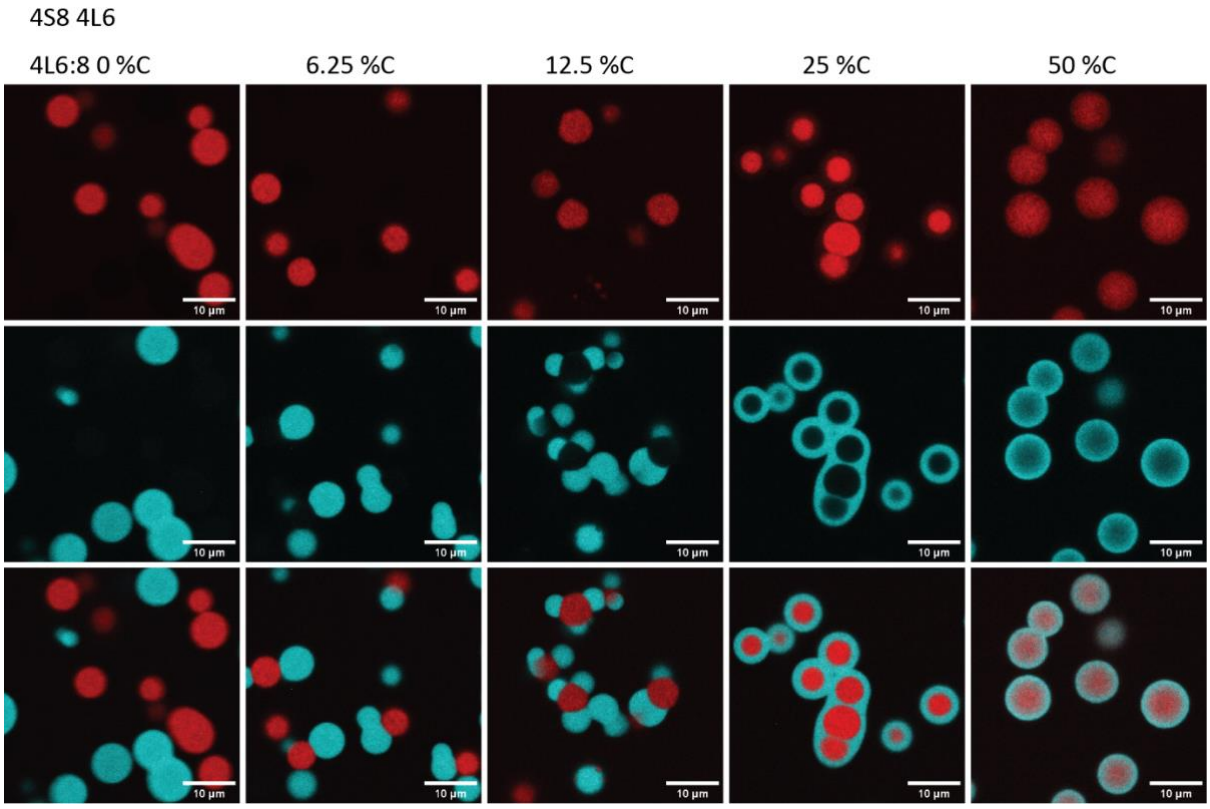

SI Figure 13: Microscale architectures upon increasing complementarity at high ΔTPS, 4S8 4L6 (17.4 °C). Droplets are false coloured red for 4S8, and cyan for 4L6. At 0 %C, there is complete separation between populations. At low degrees of complementarity, wetting of the lower T_{PS} star occurs against the high T_{PS} core. At 25 %C, core-shell structures form. At 50 %C, mixing of phases is observed, and is less homogeneous than for the 3S10 shell variant shown in SI Figure 10. Scale bars 10 µm.

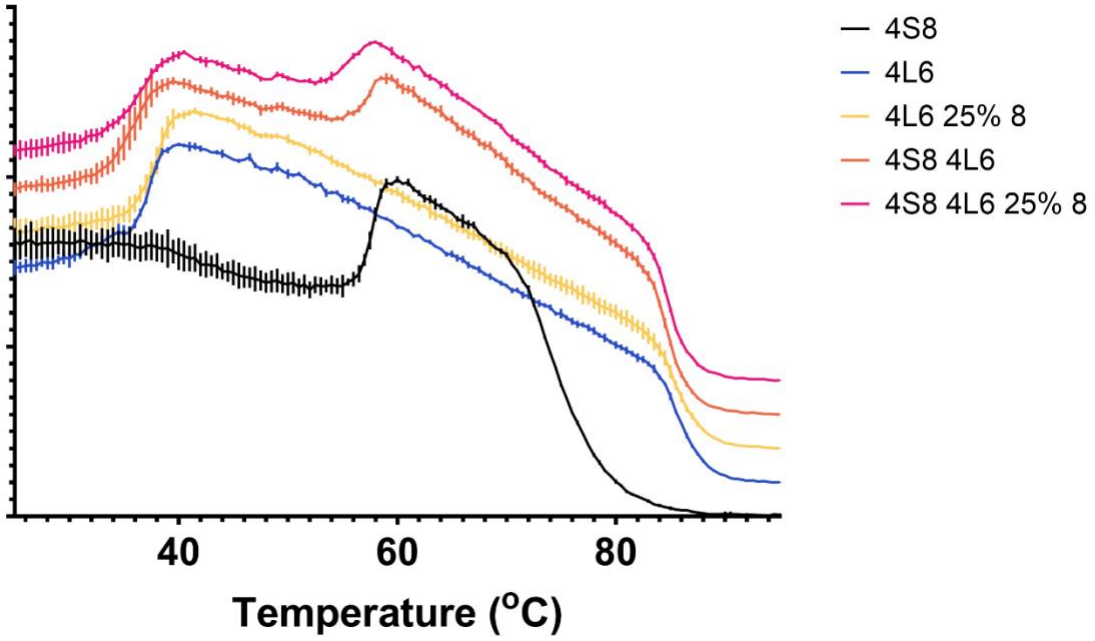

SI Figure 14: Hybridisation curves of 4S8 and 4L6 nanostars. 4L6 nanostars have 25% 8-nt SE modification, a combined solution of unmodified 4S8 and 4L6 nanostars, and a combined solution of 4S8 and 4L6 nanostars with 25% 8-nt SE modification. Curves are vertically offset for illustrative purposes. No significant difference is seen between the hybridisation curves of 4L6 and 4L6 25% 8 nanostars. Solutions containing pairs of nanostars show two incidences of phase separation, aligning with the T_{PS} of individual stars

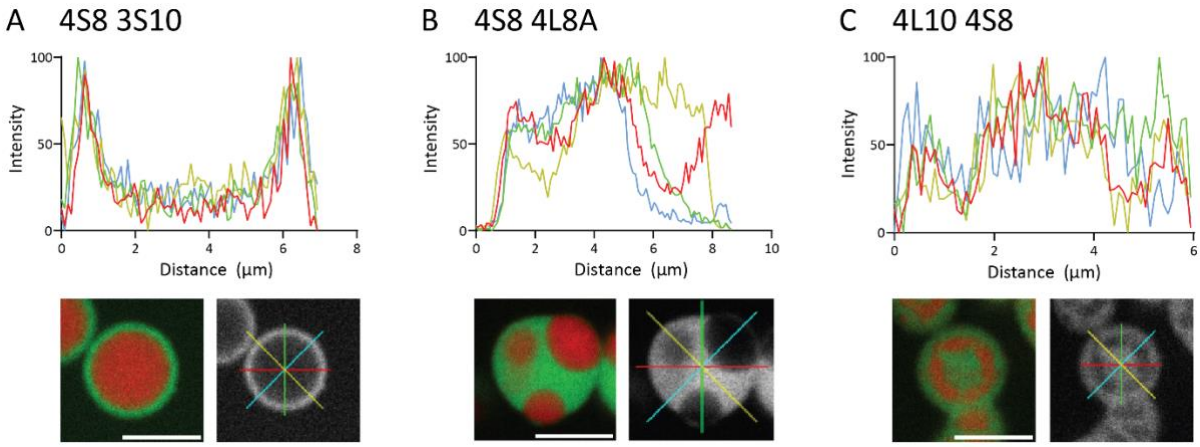

SI Figure 15: Schematic of droplet morphology analysis. To define the occurrence of shell or patchy morphologies, pixel profiles were extracted across different angles of measurement. **A** Symmetrical core-shell morphologies produced similar profiles across angles of measurement, with a high degree of correlation within a single object. Core-shell morphologies were defined as containing two distinct shell peaks, with a median profile correlation above 0.7. **B,C** Patchy morphologies had asymmetric radial profiles, with low correlation. **A-C**: Example pixel profiles of single objects in 4S8 3S10, 4S8 4L8-S, and 4L10 4S8 systems, with correlation coefficients of 0.78, 0.39, and 0.46, respectively. Scale bars 5 µm.

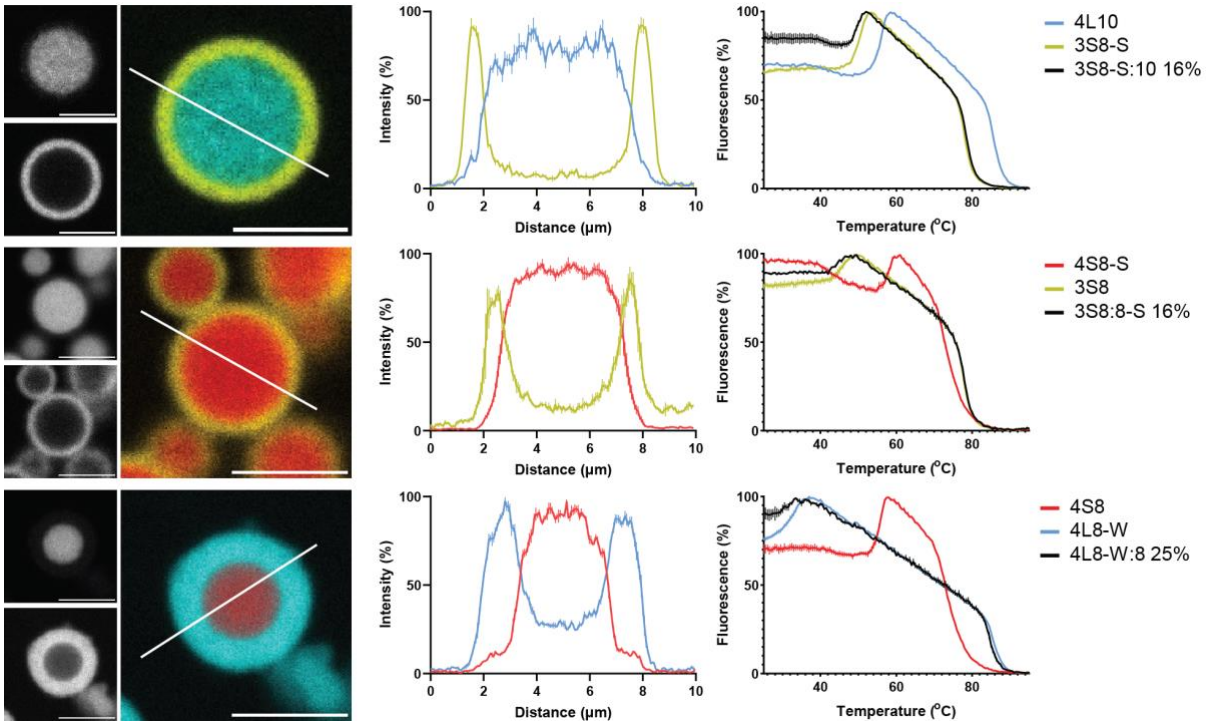

SI Figure 16: Additional examples of core-shell nanostar droplets, showing core, shell, and composite channels. Pixel intensity profiles show distinct separation between layers. Hybridisation curves show minimal difference in T_{PS} between unmodified shell and surfactant stars. Scale bars 5 µm.

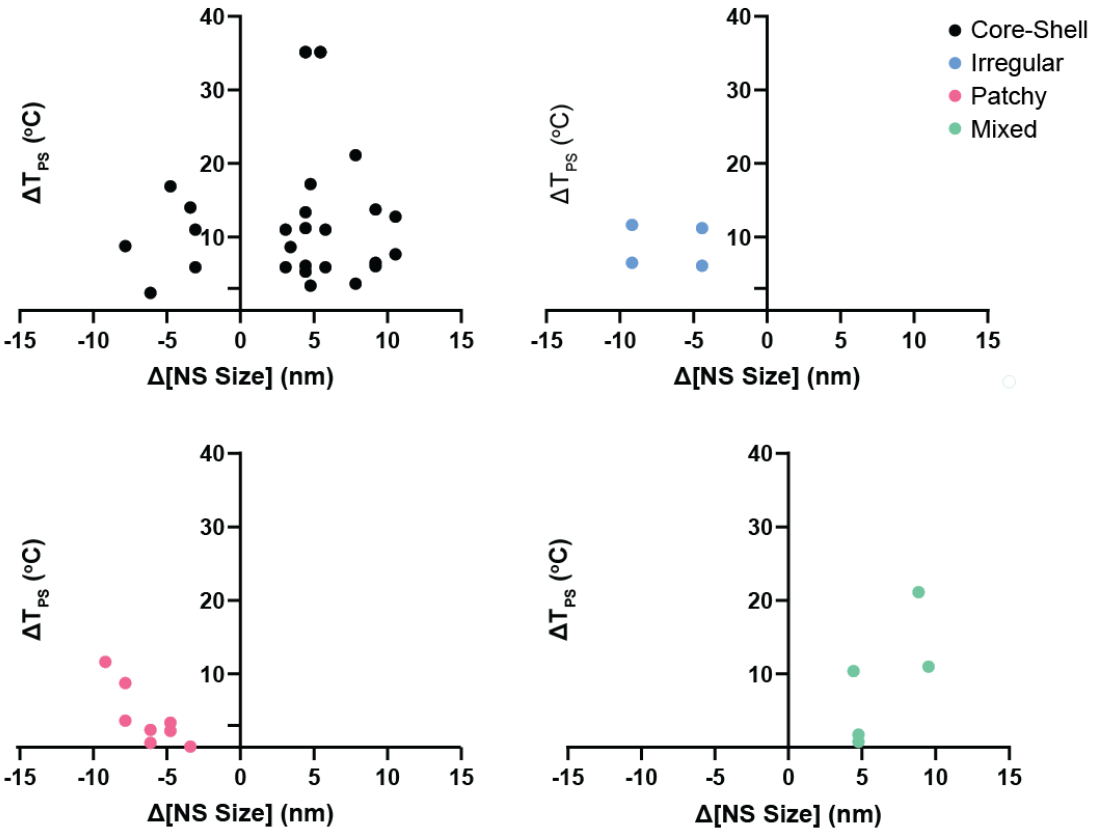

SI Figure 17: Morphology dependence on NS size difference ($S_{high\text{-}T\_PS}$ - $S_{low\text{-}T\_PS}$) and ΔT_{PS} on incidence of core-shell (black), irregular (blue), patchy (pink), or mixed (green) structure formation. Each structure is plotted individually to reveal overlapping points. Horizontal line at ΔT_{PS} = 3 °C.

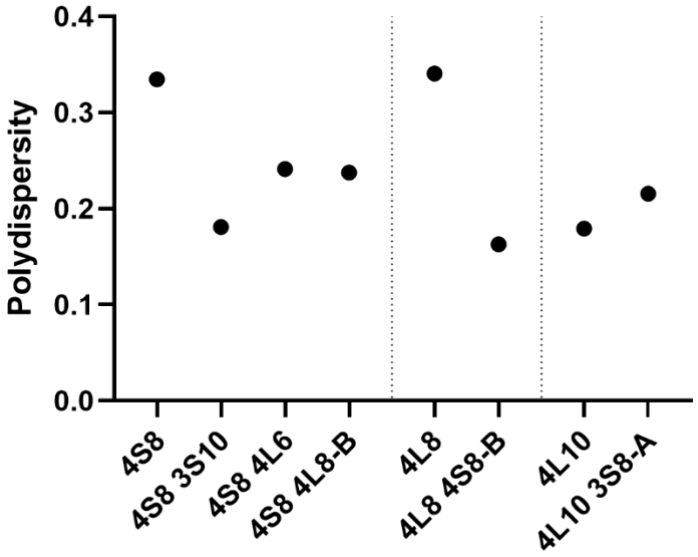

SI Figure 18: Polydispersity index of droplets (standard deviation normalised to mean) of core-only and core-shell droplets, showing decreased polydispersity in layered systems for 4S8 and 4L8 data sets.

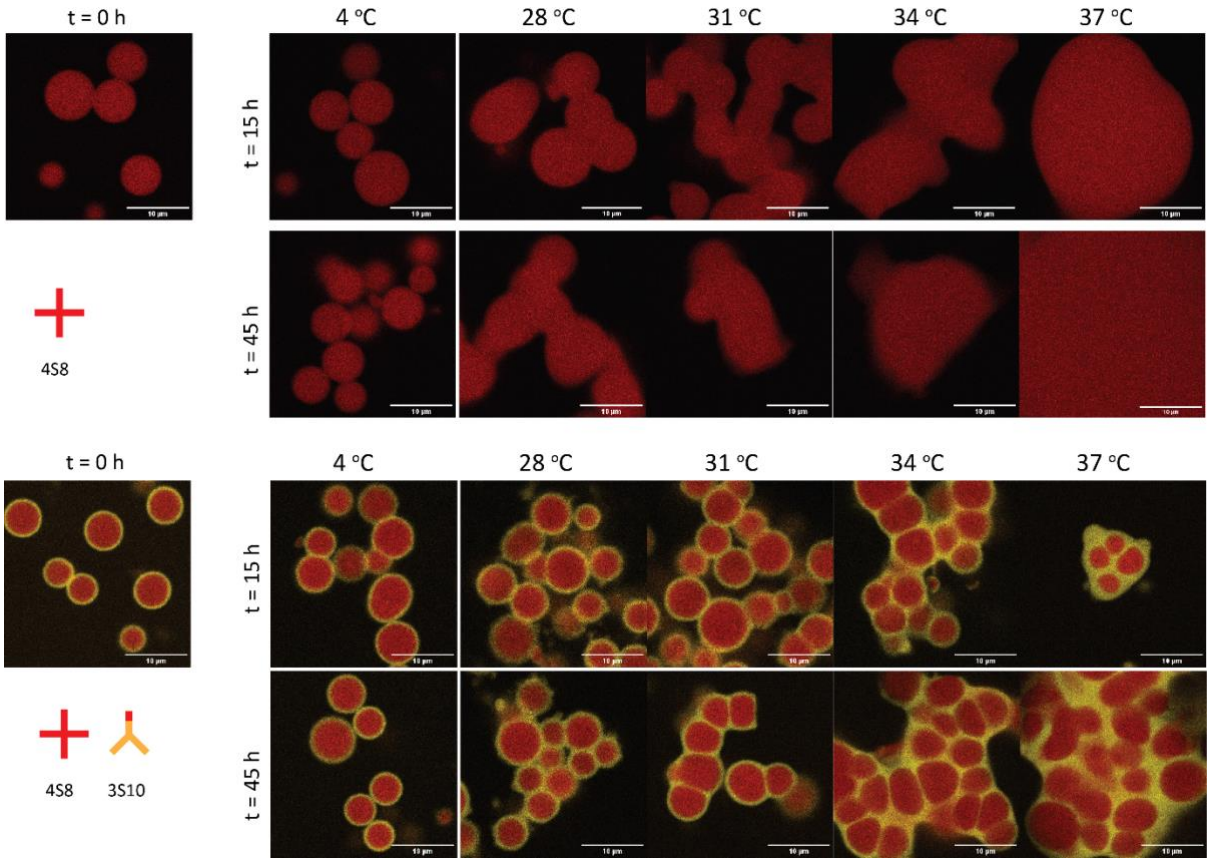

SI Figure 19: Incubation of core-only 4S8 droplets and core-shell 4S8 3S10 droplets, prepared at 10 μm and 0.5 M NaCl, were incubated at a range of temperatures for 45 hours. Fluidity in the system is defined as the propensity of droplets to fuse. Bare droplets at 4 oC show no difference to initial samples; from 28 °C onwards, core-only droplets fuse into extended structures within 15 hours, and by 37 °C show complete fusion. In core-shell systems, cores show little change up to 31 °C, indicating a shell of reduced deformability. At 34 °C, shells fuse and liquid cores are deformed. At 37 °C y at 45 h., individual shells merge and there is evidence of core fusion, indicating increased fluidity in both core and shell. Scale bars 10 μm.

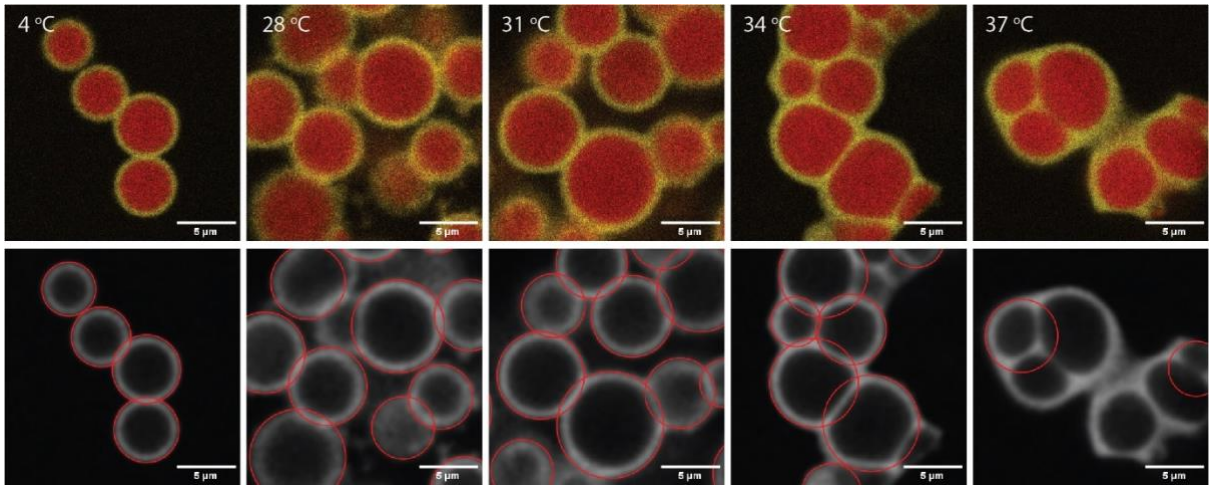

SI Figure 20: Droplet analysis by Circle Hough Transform. 4S8 3S10 droplets, incubated from 4 – 37 oC for fifteen hours, with circular structures identified by applying a Circle Hough Transform algorithm to the shell channel. Increased deformation of adjacent droplets leads to an increase in measured intersection area between adjacent circles. Outlier measurements, identified using ROUT non-linear regression (Q = 1%), were removed. Scale bars 5 µm.